Supplementary information

Declining tropical cyclone frequency under global warming

SUPPLEMENTARY INFORMATION

Declining tropical cyclone frequency under global warming

Savin S. Chand[1] *, Kevin J. E. Walsh[2], Suzana J. Camargo[3], James P. Kossin[4,5], Kevin J. Tory[6], Michael F. Wehner[7], Johnny C. L. Chan[8], Philip J. Klotzbach[9], Andrew J. Dowdy[6], Samuel S. Bell[6], Hamish A. Ramsay[10] and Hiroyuki Murakami[11]

[1]Institute of Innovation, Science and Sustainability, Federation University, Ballarat, Victoria, Australia.

[2]University of Melbourne, Parkville, Victoria, Australia.

[3]Lamont-Doherty Earth Observatory, Columbia University, Palisades, NY, USA

[4]NOAA/National Centers for Environmental Information/Climate Science and Services Division, Madison, WI, USA

[5]The Climate Service, Madison, WI, USA

[6]Research and Development Branch, Bureau of Meteorology, Melbourne, Victoria, Australia ·

[7]Lawrence Berkeley National Laboratory, Berkeley, CA, USA.

[8]Guy Carpenter Asia-Pacific Climate Impact Centre, City University of Hong Kong, Kowloon, China.

[9]Department of Atmospheric Science, Colorado State University, Fort Collins, CO, USA

[10]CSIRO, Oceans and Atmosphere, Aspendale, Victoria, Australia.

[11]National Oceanic and Atmospheric Administration/Geophysical Fluid Dynamics Laboratory, Princeton, NJ, USA.

Corresponding author address: Savin S. Chand, Institute of Innovation, Science and Sustainability, Federation University Australia, PO Box 663, Ballarat, VIC, 3353, Australia.
E-mail: **s.chand@federation.edu.au**

TC detection and tracking in reanalyses using the OWZ scheme.

We employ an innovative TC detection and tracking scheme to detect and tracks TCs in reanalyses datasets. The scheme utilizes absolute vorticity and the Okubo-Weiss Parameter normalized by the vertical component of absolute vorticity, referred to as the Okubo-Weiss-Zeta (OWZ), such that:

$OWZ = sgn(f) \times (\zeta + f) \times max[\frac{\zeta^2 - (E^2 + F^2)}{\zeta^2}, 0]$, where f is the Coriolis term, $\zeta = \frac{\partial v}{\partial x} - \frac{\partial u}{\partial y}$ is the vertical component of relative vorticity, $E = \frac{\partial u}{\partial x} - \frac{\partial v}{\partial y}$ is the stretching deformation and $F = \frac{\partial v}{\partial x} + \frac{\partial u}{\partial y}$ is the shearing deformation. The term is multiplied by the sign of f to ensure positive values for cyclonic flow in both hemispheres. Only positive values of the normalized OWZ are included such that it ranges from 1 for solid body rotation to zero when deformation exceeds vorticity. Thus, the OWZ is essentially the absolute vorticity scaled by the degree of deformation in the flow (for example, $OWZ = 0$ for pure shear vorticity, and $OWZ = \zeta + f$ for solid body rotation). The OWZ detection procedure is summarized in the following steps:

1. The reanalysis data are interpolated to a 1º × 1º grid for consistency.

2. The OWZ, relative humidity and wind shear are tested in the lower half of the troposphere and each grid point is assessed to see if it is likely to be part of a circulation that would support TC formation.

3. The "likely" grid points from step (2) are grouped into individual circulations at an instant in time.

4. The instantaneous circulations from step (3) are linked progressively in time to produce a set of storm tracks.

5. Each storm track is assessed to see whether it satisfies a set of conditions for a minimum consecutive time period of 48 h. These conditions include the following thresholds:

   - OWZ at 850-hPa: $>60 \times 10^{-6}$ s^{-1}.

   - OWZ at 500-hPa: $>50 \times 10^{-6}$ s^{-1}.

   - Relative humidity at 950-hPa: $>85\%$

   - Relative humidity at 700-hPa: $>70\%$

   - Vertical wind shear between 850- and 200-hPa: <12.5 m s^{-1}.

   - Specific humidity at 950-hPa: >14 g kg^{-1}.

   - Storms forming near or poleward of the subtropical jet are deemed to be subtropical and are therefore removed from the analysis.

Developing Bayesian model for TC counts

We suppose that TC numbers y_i in each basin are well approximated by a Poisson distribution $y_i \sim Poisson\ (\lambda_i)$, where λ_i describes the mean (and variance) of the number of TCs. A canonical link function (natural logarithmic in the case of a Poisson Generalized Linear Model) is used to relate λ_i to indices for all potential explanatory variables $\boldsymbol{X_i}$ that affect TC trends and variability in each basin such that $\ln(\lambda_i) = \beta_0 + \boldsymbol{\beta X_i}$. Here β_0 represents the intercept of the model and $\boldsymbol{\beta}$ is the vector of coefficients associated with the respective standardized explanatory variables $\boldsymbol{X_i}$. Note also that $\boldsymbol{X_i}$ comprises indices associated with the linear temporal trend (t), as well as several

modes of natural variability that modulate TC variability in different basins such as El

Niño Southern Oscillation (represented by the ENSO Longitude Index, ELI), the Indian

Ocean Dipole Index (IOD), the Pacific Decadal Oscillation (PDO), the Atlantic

Meridional Overturning Circulation (AMOC) and the North Atlantic Oscillation (NAO)

such that $X_i \in \{t_i, ELI_i, IOD_i, PDO_i, AMOC_i, NAO_i\}$ and their respective model parameters

are $\beta \in \{\beta_0, \beta_{time}, \beta_{ELI}, \beta_{IOD}, \beta_{PDO}, \beta_{AMOC}, \beta_{NAO}\}$. The posterior distribution of these model

parameters are obtained using the Gibbs sampler (see ref. 65 for details on the

implementation of the Gibbs sampler in the context of TC modelling), initialized with

standard noninformative priors (i.e. mean of 0 and variance of 10^6). This very large

variance indicates very small precision (i.e., 10^{-6}) and thus contributes little information

about the data. Altogether, we performed 50,000 iterations with the first 5,000 discarded

as a "burn-in" required for the model to reach stability (as determined using standard

diagnostics, not shown). For the remaining iterations, we only considered every 5th

iteration to ensure that any influence from potential autocorrelation is removed. This

leaves us with 9,000 iterations that were used to construct the posterior density

distribution of each model parameter.

Table S1. Hit rate and false alarm rate of TCs detected in 20CR and IBTrACS for the period 1989-2012. The hit rate is the ratio of the number of hits divided by the total number of TCs observed, with a value of 1 representing a perfect score. Similarly, the false alarm rate is the ratio of the number of false alarms divided by the total number of TCs detected, with a value of 0 representing a perfect score.

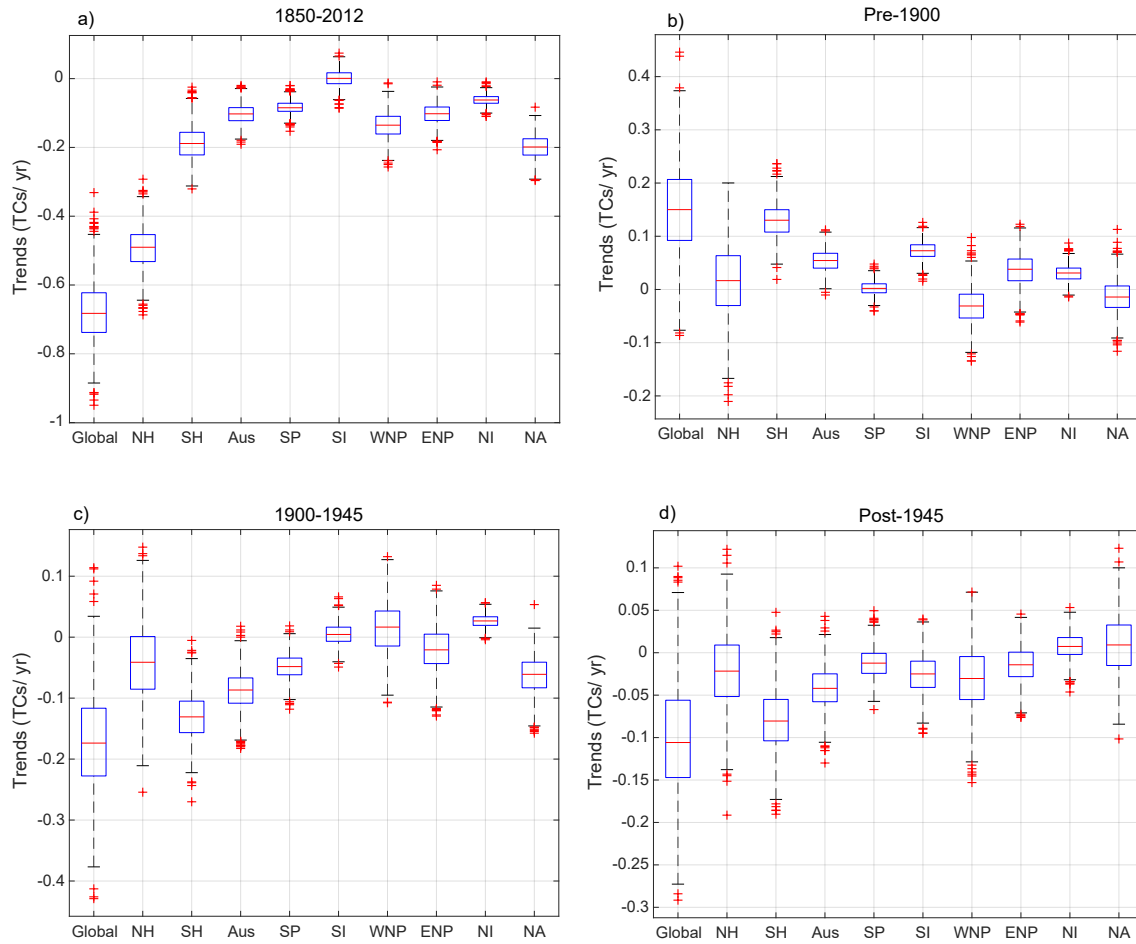| Basin	Hit rate	False alarm rate
Southern Hemisphere	0.86	0.48
Northern Hemisphere	0.74	0.39
Australian region	0.85	0.43
South Pacific	0.81	0.59
South Indian	0.90	0.56
Western North Pacific	0.87	0.27
Eastern North Pacific	0.54	0.73
North Indian	0.80	0.56
North Atlantic	0.69	0.31

Figure S1 | Bootstrap trends in annual TC numbers. a, b, c, d Boxplots of trends in annual TC numbers globally, the two hemispheres and individual basins obtained using 1000 bootstrap samples over the entire period 1850-2012 (**a**), pre-1900 (**b**), between 1900-1945 (**c**) and post-1945 (**d**).
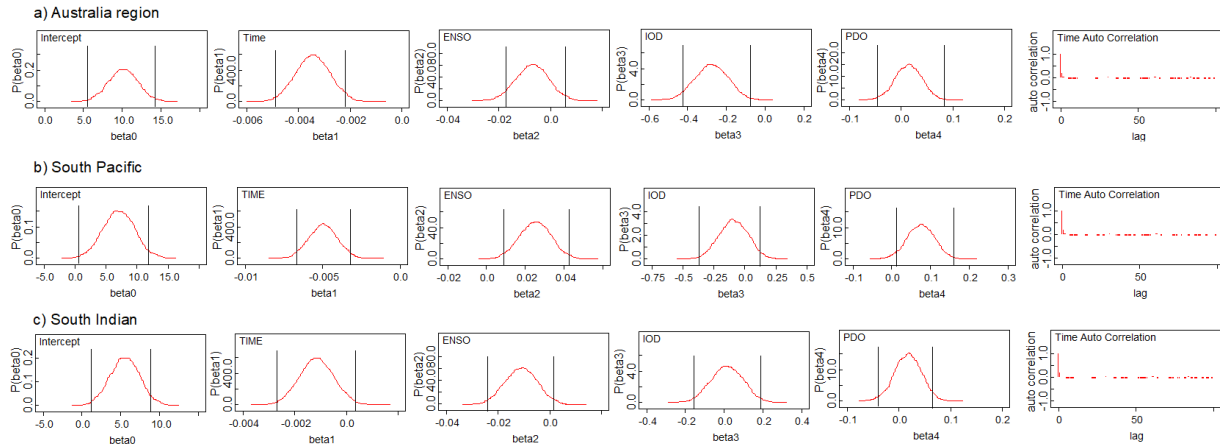
Figure S2 | Posterior density distribution plots of Bayesian regression parameters (rows) associated with the trend ('beta 1') and various other potential climate drivers that modulate annual TC numbers in the Southern Hemisphere basins. **a-c**, Australian region, South Pacific basin and South Indian basin. The vertical reference lines for each distribution enclose the 95% credible interval, which is the Bayesian equivalent of the confidence interval. 'Beta' refers to the posterior distribution associated with the different model parameters. If this credible interval lies outside the "zero" line, then the associated model parameter is deemed "statistically significant". The last column is the autocorrelation associated with the TC trend for each basin, and the values reach zero fairly quickly indicating no violation of the stationarity assumptions.
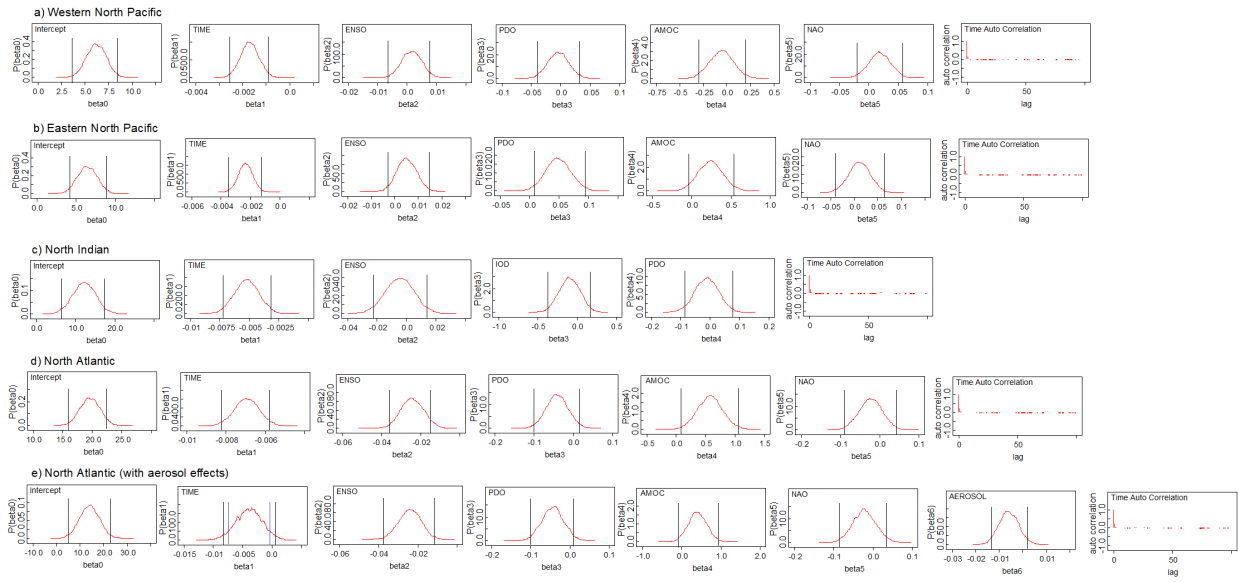
Figure S3 | As in Extended Data Fig. 2 but for the Northern Hemisphere basins. a-d, the Western North Pacific, Eastern North Pacific, North Indian and North Atlantic basins. **e**, Posterior distribution plot for the North Atlantic basin with an additional variable for aerosols where the blue line associated with beta 1 denotes the 90% credible interval.
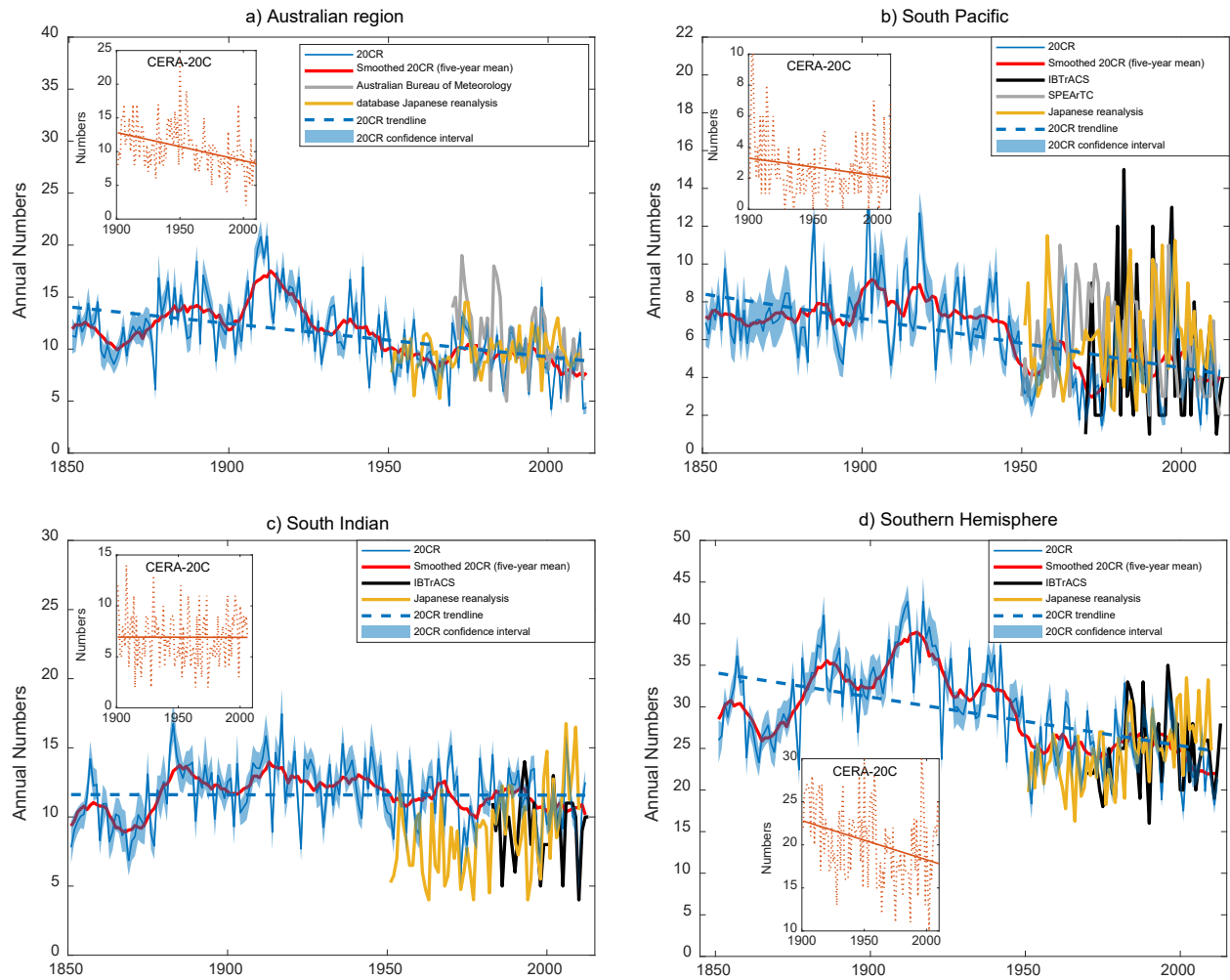
Figure S4 | Comparisons of the annual TC numbers for the Southern Hemisphere basins derived from various data sources. a-c, the Australian region, South Pacific basin and South Indian basin. **d**, The entire Southern Hemisphere. The time series derived from the 20CR comprises the ensemble-mean TC numbers for each year (blue solid line) and the associated spread at the 95% confidence interval (blue shading), the trends in the ensemble-mean annual TC numbers (blue dashed line) and the five-year running mean (red-line). Time series corresponding to IBTrACS (black line), MRI-AGCM3.2-derived historical simulations (referred to as the Japanese reanalysis, orange line) and other basin-specific local sources (such as the Australian Bureau of Meteorology for the Australian region and SPEArTC for the South Pacific basin, grey lines) are also shown. The insert on each figure shows the time series of annual TC numbers for the period 1901-2010, derived from CERA-20C.
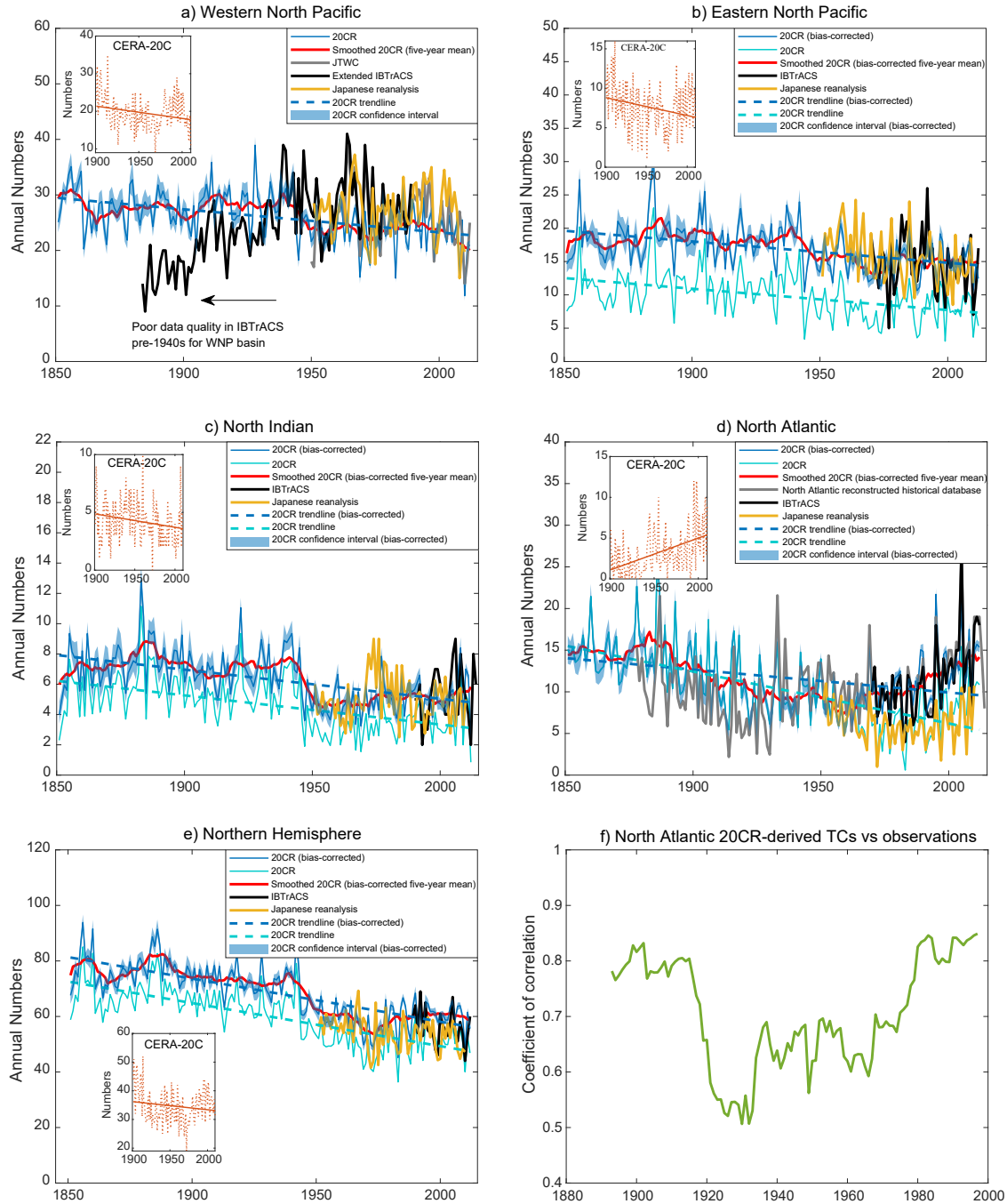
9

Figure S5 | As in Extended Data Fig. 4 but for the Northern Hemisphere basins. a-d, the Western North Pacific, Eastern North Pacific, North Indian and North Atlantic basins. **e**, Entire Northern Hemisphere. Note here that we have included both the bias-corrected time series (blue) and the "original time series" (cyan lines) for the 20CR. **f**, Fifteen-year running correlation coefficient between the 20CR and reconstructed historical annual TC numbers for the North Atlantic basin.
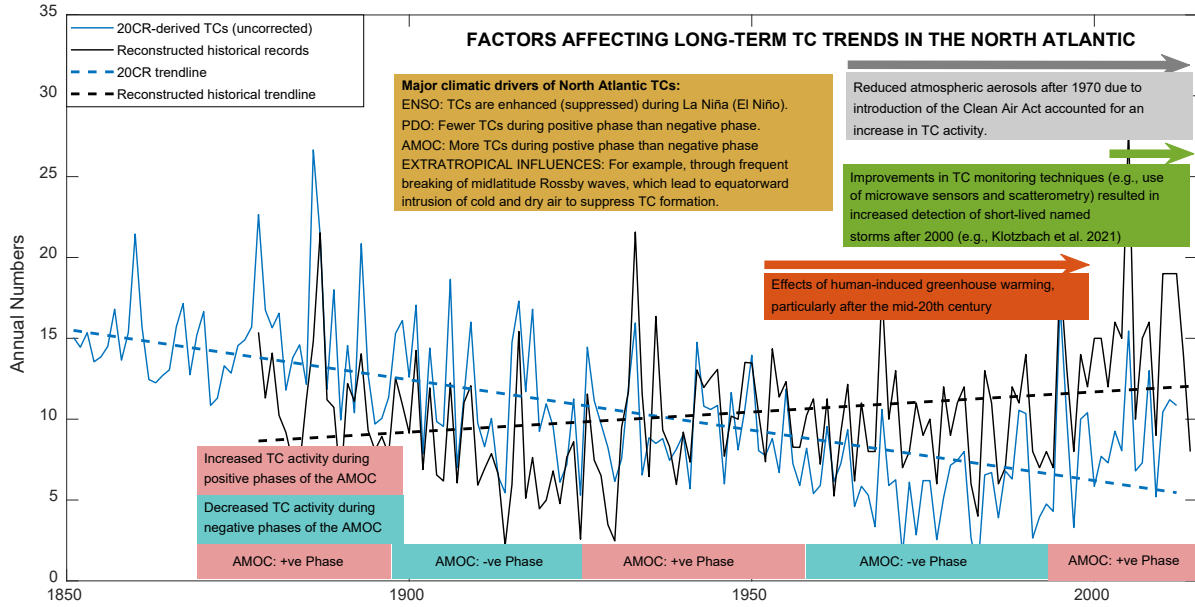
FACTORS AFFECTING LONG-TERM TC TRENDS IN THE NORTH ATLANTIC

Reduced atmospheric aerosols after 1970 due to introduction of the Clean Air Act accounted for an increase in TC activity.

Major climatic drivers of North Atlantic TCs:
ENSO: TCs are enhanced (suppressed) during La Niña (El Niño).
PDO: Fewer TCs during positive phase than negative phase.
AMOC: More TCs during postive phase than negative phase
EXTRATROPICAL INFLUENCES: For example, through frequent breaking of midlatitude Rossby waves, which lead to equatorward intrusion of cold and dry air to suppress TC formation.

Improvements in TC monitoring techniques (e.g., use of microwave sensors and scatterometry) resulted in increased detection of short-lived named storms after 2000 (e.g., Klotzbach et al. 2021)

Effects of human-induced greenhouse warming, particularly after the mid-20th century

Increased TC activity during positive phases of the AMOC

Decreased TC activity during negative phases of the AMOC

AMOC: +ve Phase | AMOC: -ve Phase | AMOC: +ve Phase | AMOC: -ve Phase | AMOC: +ve Phase

Legend:
— 20CR-derived TCs (uncorrected)
— Reconstructed historical records
- - 20CR trendline
- - Reconstructed historical trendline

Figure S6 | Schematic summarizing various factors affecting long-term North Atlantic TC trends. The time series derived from the 20CR comprises the ensemble-mean TC numbers for each year (blue solid line) and the associated trendline (blue dashed line). Time series corresponding to the reconstructed historical TCs (and the associated trendline) obtained from the US National Hurricane Center database for the period 1878 onwards are also shown (black lines).
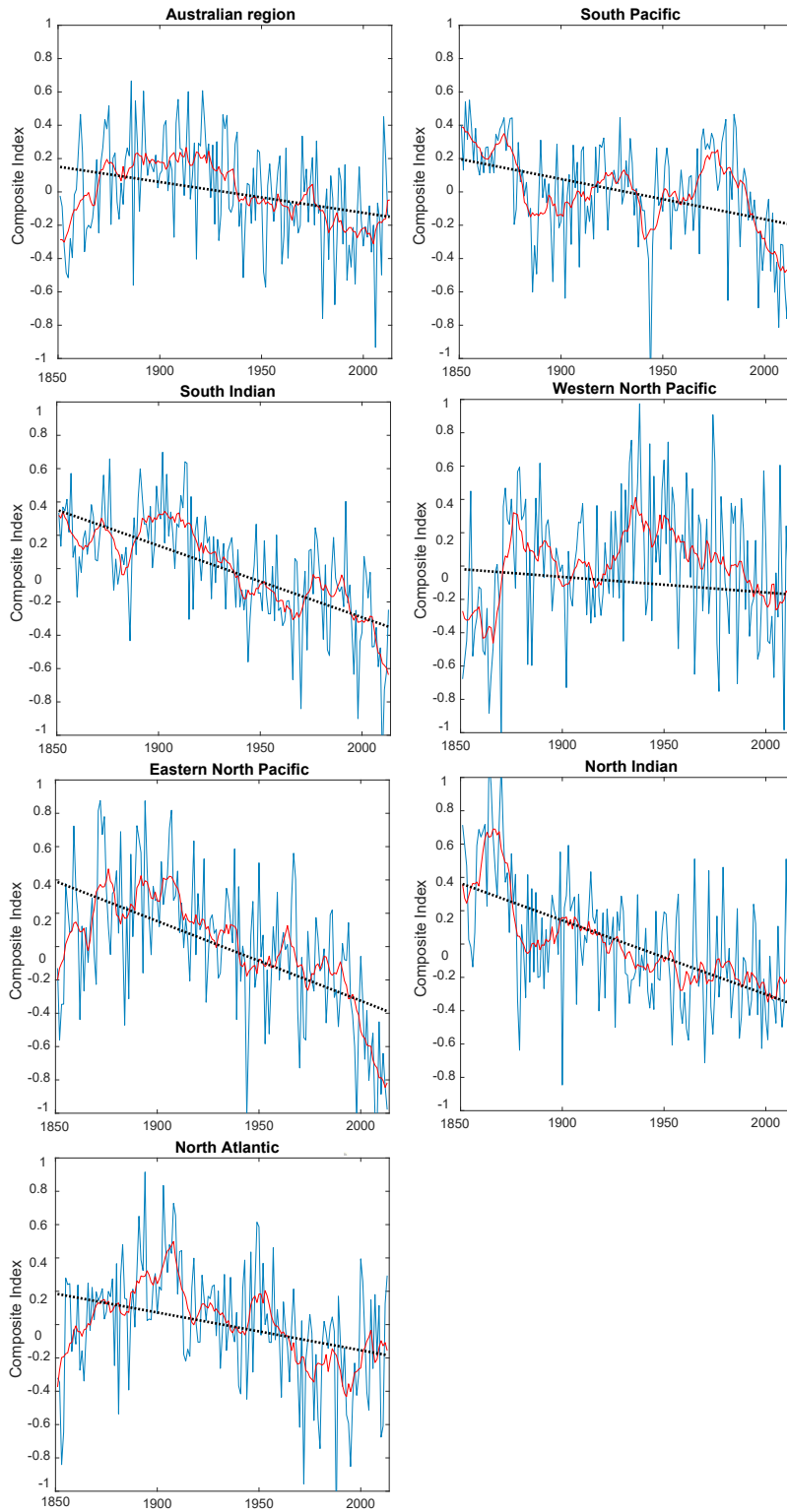
Figure S7 | Normalized composite index derived from large-scale environmental conditions for all TC basins. The time series of the annual composite index (blue solid line), the associated trendline (black dotted line) and the five-year running mean (red-line).
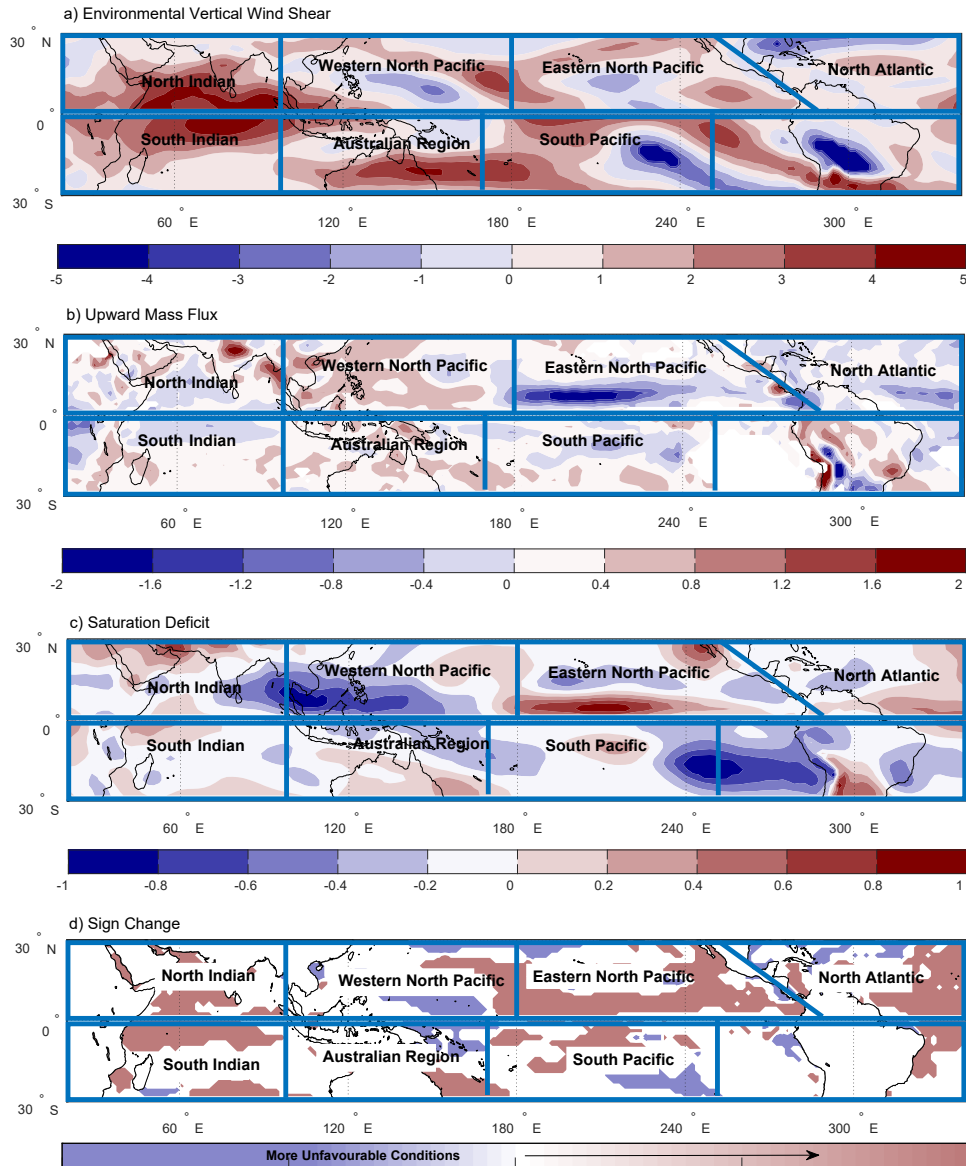
Figure S8 | Mean changes in large-scale environmental conditions (derived from 20CR) between the two climate periods: historical (1951-2010) minus pre-industrial (1851-1900). a, environmental vertical wind shear between the 850- and 200-hPa levels (m s^{-1}). **b,** the 600-hPa upward mass flux (hPa h[-1]). **c**, the 600-hPa saturation deficit (g kg^{-1}) **d**, the sign-change in the majority of environmental conditions that become more unfavorable for TC formation between the two climate periods.
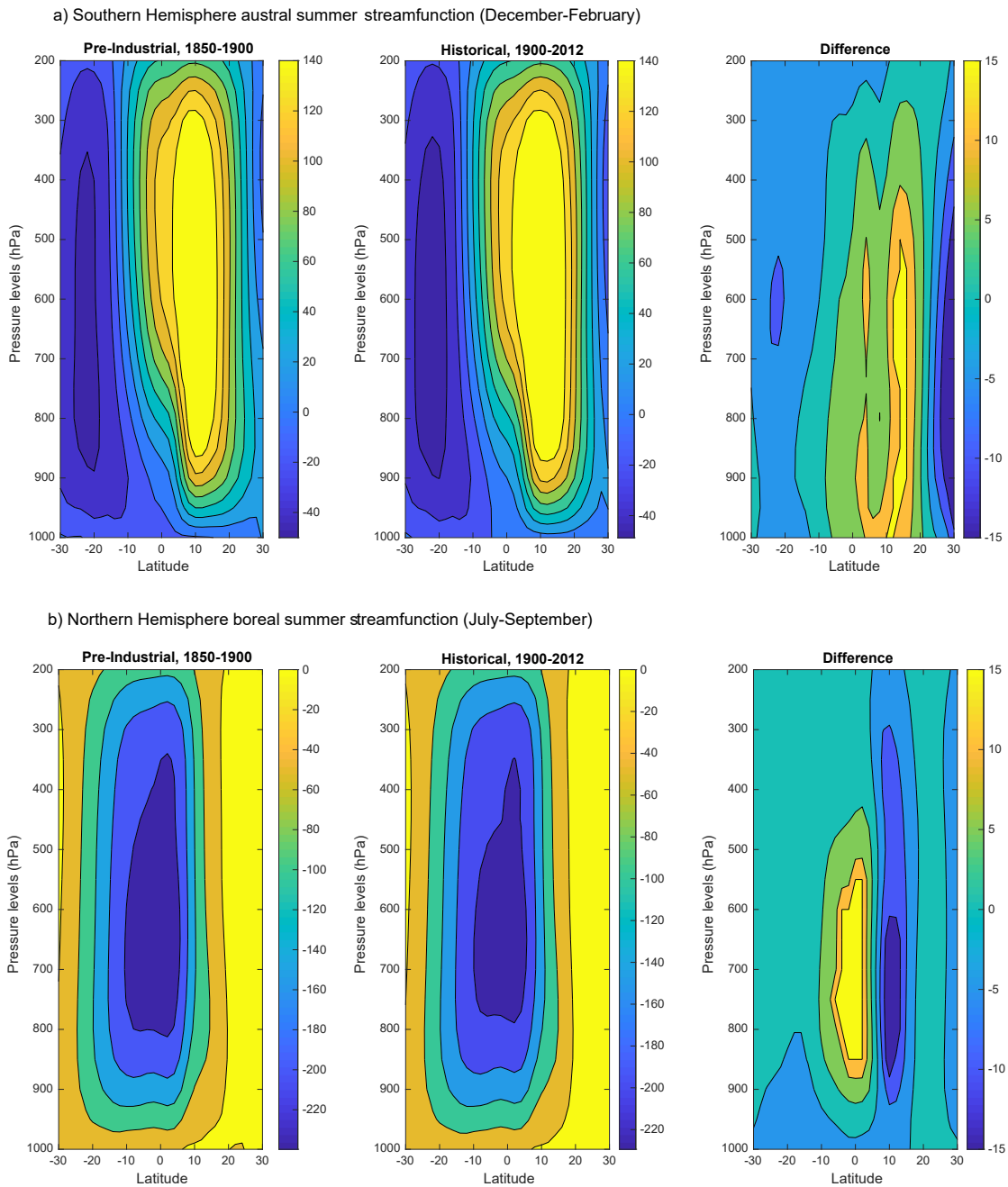
a) Southern Hemisphere austral summer streamfunction (December-February)

b) Northern Hemisphere boreal summer streamfunction (July-September)

Figure S9 | Cross-section of mass streamfunctions, Ψ, of the zonal mean meridional circulation derived from the 20CR dataset (10^9 kg s^{-1}). a Southern Hemisphere austral summer (i.e., December-February) composite streamfunction for pre-industrial (1850-1900) and historical periods (1950-2012), and their difference (historical minus pre-industrial). **b** Same as (a) but for the Northern Hemisphere boreal summer (July-September, JAS). Note the negative (positive) values of Ψ for pre-industrial and historical indicate an anticlockwise (clockwise) circulation. Negative (positive) values of Ψ for the difference plot indicate a weakening of the circulation in the Northern (Southern) hemisphere latitudes.
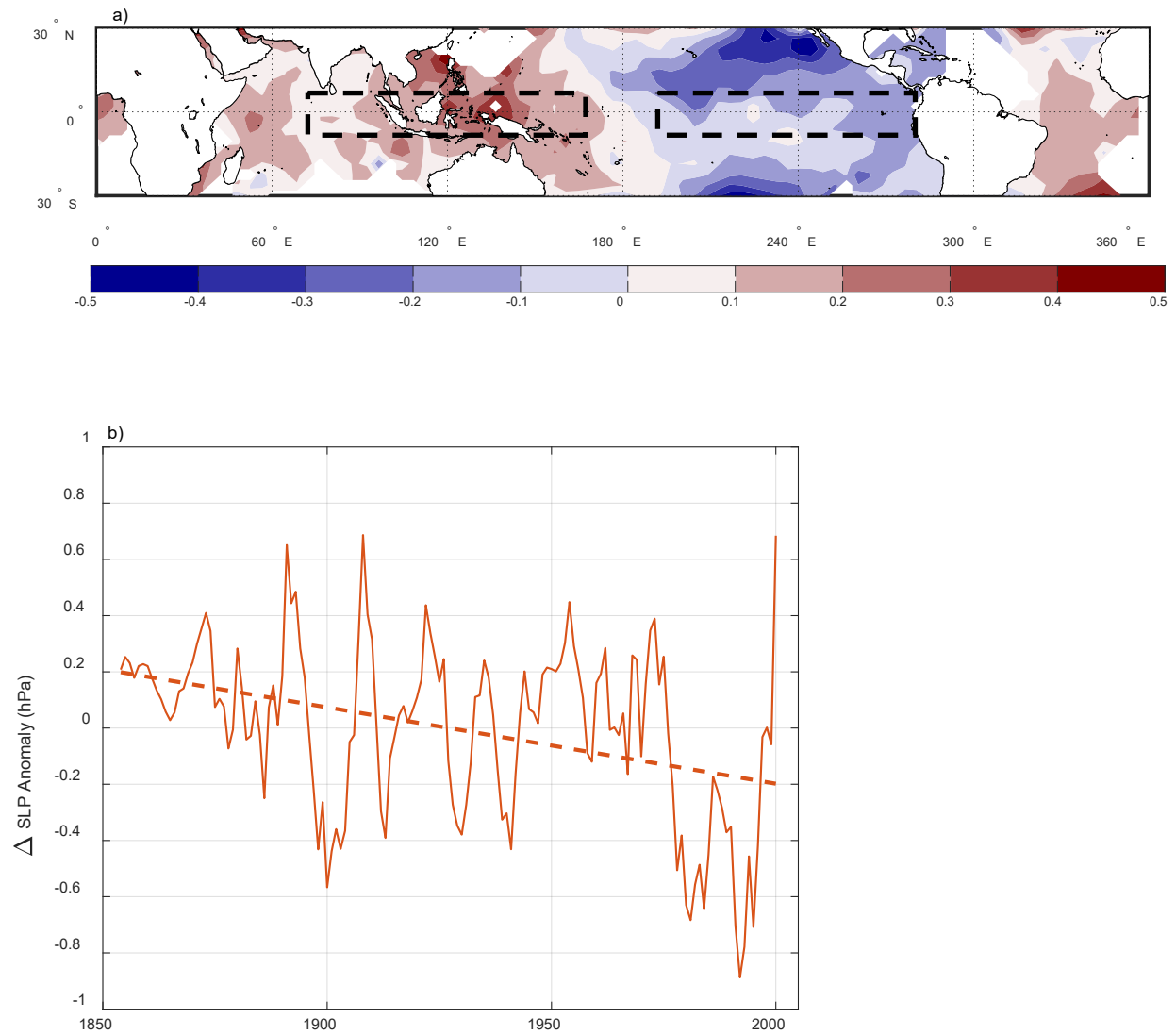
14

Figure S10 | Spatial pattern of observed sea level pressure (SLP) trends and the associated ΔSLP that is used as a proxy to define the strength of the Walker Circulation. a SLP linear trends (dashed black rectangles are used to define the Indo-Pacific SLP gradient, ΔSLP, which serves as a proxy of changes in mean intensity of the Pacific Walker Circulation). **b** Changes in the Indo-Pacific SLP gradient since the mid-nineteenth century.
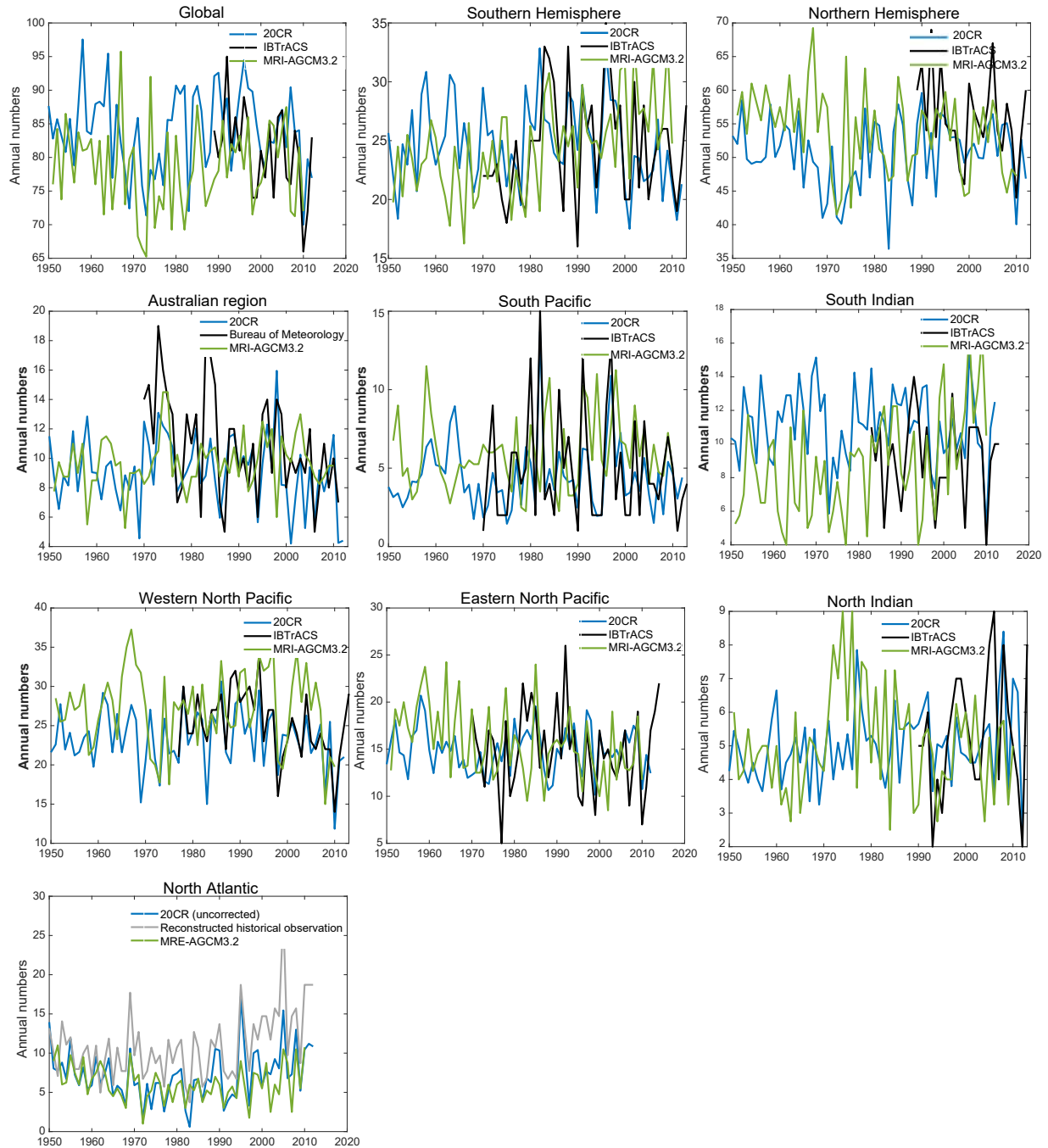
Figure S11 | Comparisons of annual TC numbers derived using different tracking schemes. The 20CR-derived TCs (obtained via the OWZ tracking scheme, blue lines) versus the MRI-AGCM3.2 simulated TCs (obtained via a scheme detailed in Murakami et al. 2012, green lines) for the period 1950-2012. TCs from the observationally-based sources are also shown (IBTrACS, black lines and HURDAT2 for the North Atlantic, grey line).
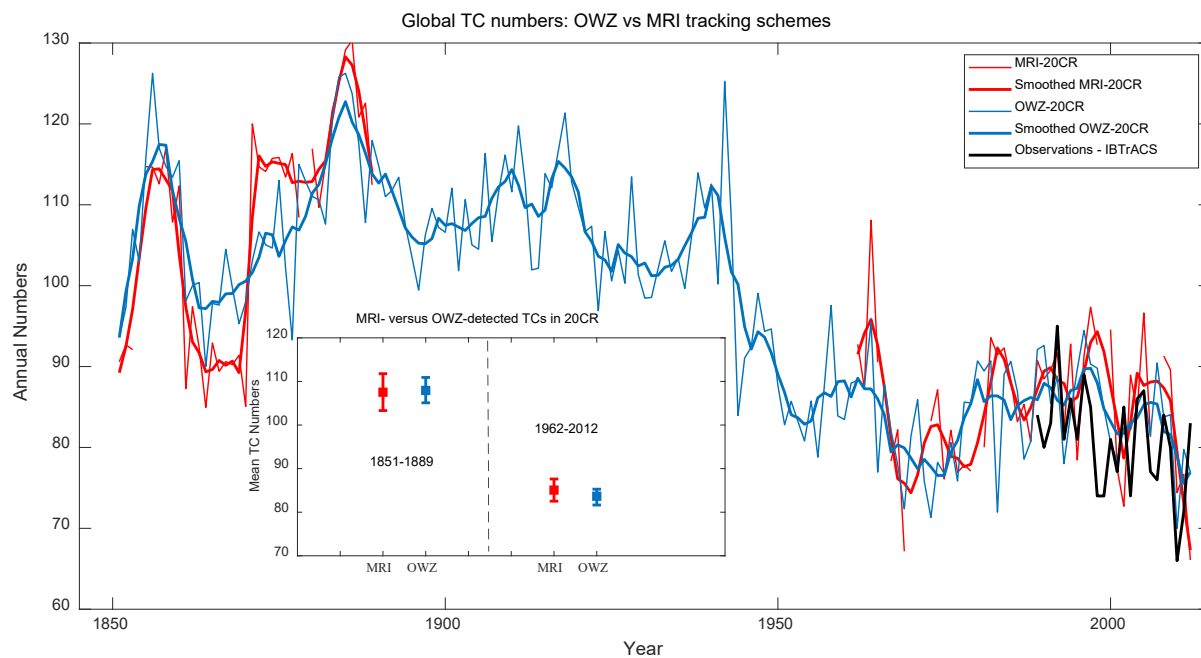
Figure S12 | Comparisons of annual TC numbers derived using the OWZ and MRI tracking schemes in the 20CR dataset over the 1851-1889 and 1962-2012 periods. The OWZ-derived TCs (blue lines) versus the MRI-derived TCs (obtained via a scheme detailed in Murakami et al. 2012, red lines) for the two comparison periods, 1851-1889 and 1962-2012, as well as observed TCs from the IBTrACS (black lines), are shown. The insert shows bootstrap confidence intervals of the ensemble mean number of TCs (at the 95% significance level) for each tracking scheme during the two periods.
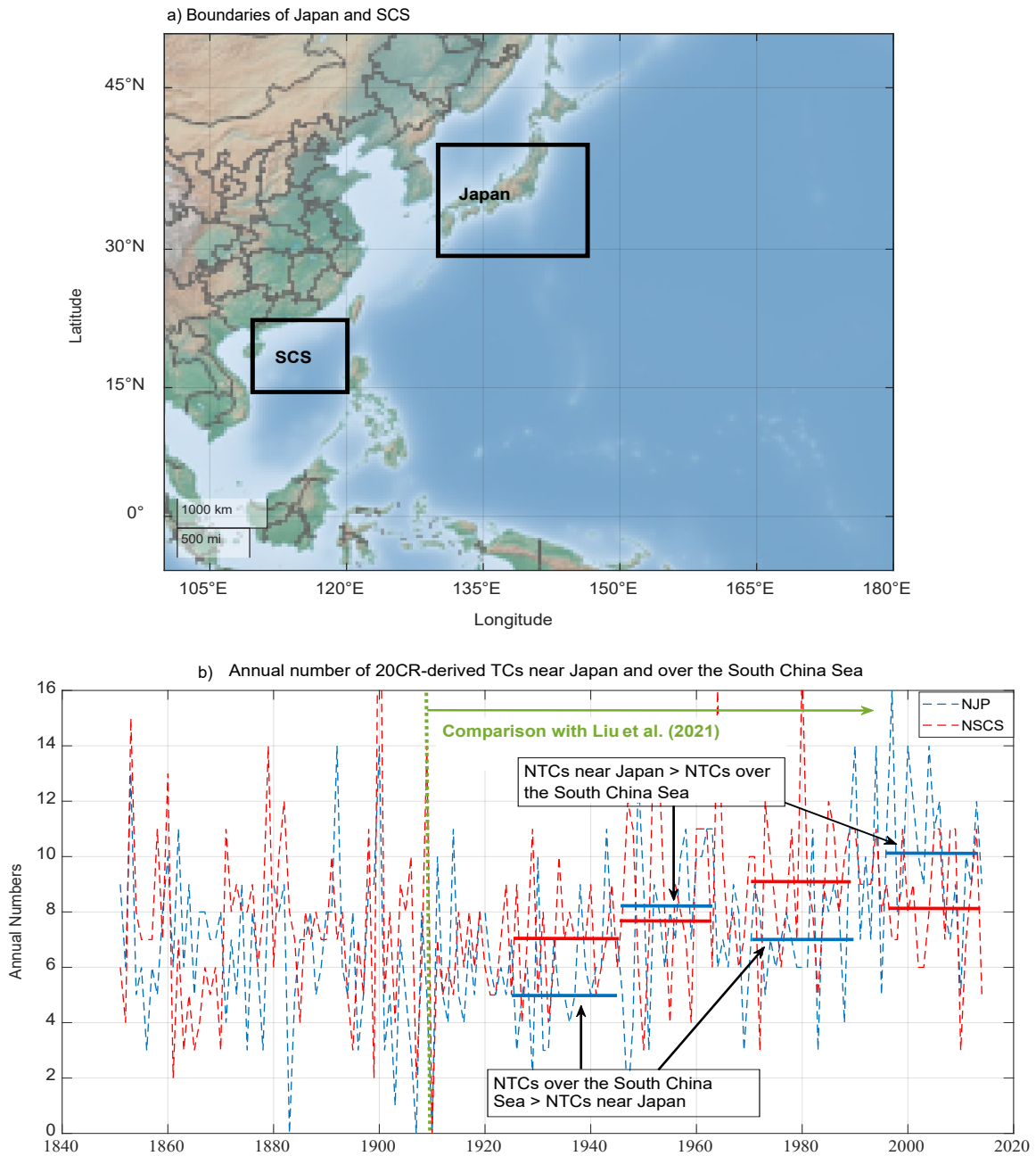
a) Boundaries of Japan and SCS

b) Annual number of 20CR-derived TCs near Japan and over the South China Sea

Figure S13 | Meridional oscillation of 20CR-derived TCs over Japan and the South China Sea (SCS). a, Map of the Western North Pacific basin showing boundaries used to define the Japan and SCS regions. **b**, Meridional oscillation of TCs derived from 20CR. Refer to Figures 2e and 2d in Liu et al. (2021) for comparisons of their meridional oscillation results with those in (b) above.